

# Numerical method for thermal donors formation simulation during silicon Czochralski growth

M. Chatelain, M. Albaric<sup>\*</sup>, D. Pelletier, J. Veirman, E. Letty

Univ Grenoble Alpes, CEA, LITEN, INES, 50 avenue du Lac Léman, F-73375, Le Bourget-du-Lac, France

## ARTICLE INFO

### Keywords:

Thermal donors  
Silicon  
Czochralski  
Crystal growth  
Simulation

## ABSTRACT

Various upgrades of the Czochralski (Cz) growth process are currently being investigated in order to increase throughput and reduce production cost of high efficiency silicon-based solar cells. However, as-grown thermal donors (TD) in Cz silicon can significantly reduce the conversion efficiency of such solar cells. An accurate simulation tool is therefore required to investigate and optimize TD formation during crystal growth. A numerical method combining thermo-hydraulic simulations and a kinetic TD formation model was improved by the implementation of a more appropriate TD formation model, identified through a benchmark of the different models available in the literature. Three different Cz growth processes were investigated both numerically and experimentally. Numerical results are in remarkable agreement with TD concentrations measured along the three ingots by the OxyMap technique developed at CEA. The simulations were then used to detect when TD were formed during Cz processes. The reliability of the method was also assessed through sensitivity analyses, highlighting the critical importance of the input interstitial oxygen concentration. These results show that accurate estimates of axial TD concentration profiles can be obtained and so for very different Cz processes, supporting the robustness of the developed method and its relevance to process optimization and furnace design to reduce TD concentrations.

## 1. Introduction

In a context of fierce competition, improving wafer quality is essential for the production of cost-effective high efficiency silicon-based photovoltaic solar cells. To reach high efficiencies, Czochralski (Cz) silicon wafers are widely used for their long minority carrier lifetimes [1]. The minority carrier lifetime is however limited by crystal defects, such as thermal donors (TD) formed during ingot growth and cooling [2,3]. TD are believed to be small chains resulting from the aggregation of a few atoms of silicon (Si) and interstitial oxygen ( $O_i$ ) [4]. They are generated in significant amounts in a large temperature range between 350°C and 600°C [5,6]. TD concentration, [TD], is then a function of the interstitial oxygen concentration,  $[O_i]$ , and of the temperature versus time profile (or thermal history) in this range [7]. The TD formation rate was shown to increase with  $[O_i]$  and to increase with temperature until a local maximum is reached around 470°C [6]. The effects of oxygen and related defects on the solar cell performance have been intensively studied in the past decade [8,9]. It has been shown that these electrically recombination-active defects can lead to a significant

reduction of amorphous/crystalline silicon heterojunction solar cells (SHJ) efficiency [2,10]. For instance, SHJ cells efficiency can be reduced by 1% absolute for a TD concentration of  $10^{15} \text{cm}^{-3}$ , a value that can be observed in industrial Cz Si ingots. As-grown TD can then be particularly detrimental to SHJ cells [2,11] since the maximal SHJ process temperature usually remains below 240°C, which does not allow to dissolve TD. Moreover, TD may also be associated with the formation of recombination-active dark rings in both p- and n-type high temperature cell processes [12,13].

Nowadays, many upgrades of Cz growth furnaces are proposed to reduce the cost ratio (\$/W), including: new hot zone designs [14], cooling jacket [15], longer ingots and/or larger wafers [16]. These upgrades can also lead to an increase of [TD] since they directly affect the ingot thermal history. The prediction of the Cz ingot thermal history from growth parameters is then essential as it is a key parameter that governs both the bulk quality (through [TD]) and the crystallization throughput. A computation method for TD formation during Cz crystal growth and ingot cooling was recently proposed by our research team [17,18]. This method relies on thermo-hydraulic simulations to

<sup>\*</sup> Corresponding author.

E-mail address: [mickael.albaric@cea.fr](mailto:mickael.albaric@cea.fr) (M. Albaric).

determine the ingot thermal history, and on the TD formation model proposed by Wada [5] to compute [TD]. This first study pointed out several limitations of the method that were mainly related to uncertainties regarding the formulation of Wada's model [5] and its applicability for crystal growth configurations where the temperature is not constant but continuously decreasing. The assessment of the robustness of the method was also limited by the analysis of only one Cz ingot.

In the present study, this original method was used to investigate the effect of the Cz growth parameters on the TD formation dynamics. Computations were performed for three different growth configurations and the results were compared to experimental TD concentrations. In order to improve the method, a comprehensive comparison of the relevant TD formation models [5,6,19,20] was performed. Sensitivity analyses focusing on the input  $[O_i]$  and the crystal pulling rate were also performed to assess the method robustness. Following this introduction, the manuscript was structured to present in section 2 the details of Cz growth experiments and ingot characterization, and in section 3 the TD formation computation. The results are presented and discussed in section 4 and concluding remarks are given in section 5.

## 2. Experimental procedure

In this work, three Cz ingots were pulled with different growth processes (see Table 1), in our facilities with an industrial furnace (Kayex KX100). Ingots 1 and 2 weighed 90 kg for a useable length of about 1 m (the useable length referring to the ingot cylindrical part or body) and a mean diameter of about 205 mm which is close to the industrial standard. Ingot 2 was popped out during the tailing step which resulted in a smaller full length compared to ingot 1. On the other hand, ingot 3 weighed 30 kg and its useable length was about 250 mm. As a result of the significantly different growth processes used, each ingot experienced a different thermal history. Note that 'reference' growth parameters were used for ingot 1 and 'optimized' growth parameters were used for ingots 2 and 3. The 'optimized' parameters refer to an increase of the argon flow rate by a factor 1.6 and an increase of the seed rotation speed by a factor 1.4 compared to the 'reference' parameters, in order to enhance oxygen evaporation at the silicon melt free surface.

For the three experimental configurations, [TD] along the ingots were calculated from resistivity measurements obtained with an OxyMap equipment calibrated with FTIR measured samples [10]. The OxyMap technique was also used for  $[O_i]$  measurements. Its reliability for measurements on wafers allowed a high spatial resolution for axial concentration profiles and the measurement uncertainty is expected to be less than  $\pm 5\%$  [10]. FTIR measurements were also performed (according to the SEMI-recommended ASTM F1188-93a norm associated to the IOC88 calibration coefficient of  $3.14 \times 10^{17} \text{ cm}^{-2}$ ) on specific samples collected along the ingot axis, and a good agreement was observed with OxyMap data. Fig. 1 presents  $[O_i]$  profiles along the three ingots as a function of the solid fraction  $f_s$ , which is defined in this study as a fraction of the ingot body length. The three ingots featured  $[O_i]$  values comprised between  $7.1 \times 10^{17}$  and  $1.1 \times 10^{18} \text{ cm}^{-3}$ , which is representative of industrial Cz Si for solar cells (i.e. from  $5 \times 10^{17}$  to  $1 \times 10^{18} \text{ cm}^{-3}$ ).

**Table 1**  
Crystallization process parameters.

	ingot 1	ingot 2	ingot 3
Silicon load	90 kg	90 kg	30 kg
Growth parameters	reference	optimized	optimized
Feedstock	Electronic Grade		
Dopant	Phosphorus		
Mean diameter	205 mm		

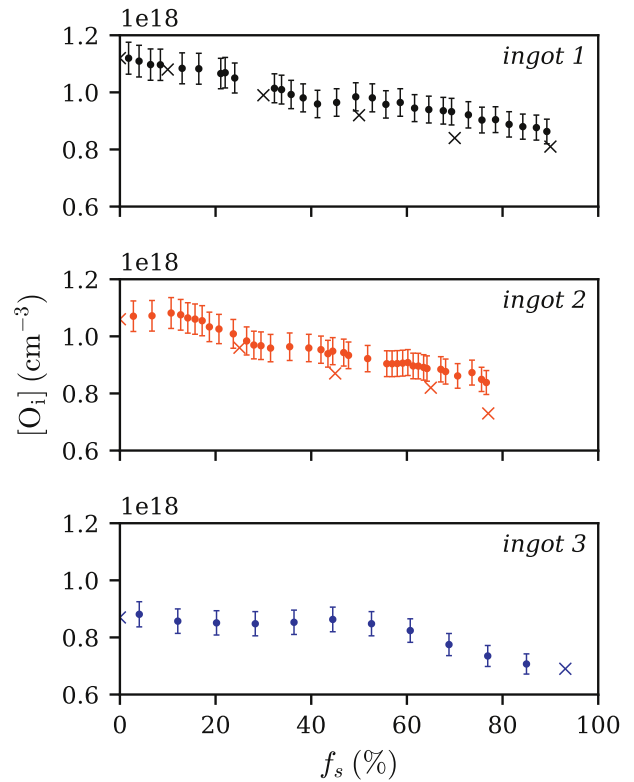


**Fig. 1.** Interstitial oxygen concentrations measured along the three ingots, with  $f_s$  the fraction of the ingot body length. Points (•) represent OxyMap measurements and crosses (×) FTIR measurements. Error bars represent a measurement uncertainty of  $\pm 5\%$  associated to the OxyMap technique [10].

## 3. Numerical procedure

### 3.1. Procedure overview

An original method to compute TD formation during Cz growth was recently proposed by Veirman et al. [18]. This method combines thermo-hydraulic simulations, providing the ingot thermal history, and an empirical TD formation model proposed by Wada [5]. The TD formation model defines the formation rate,  $G \text{ (cm}^{-3} \text{ s}^{-1}\text{)}$ , as a function of  $T$  and  $[O_i]$ . The final [TD] at each ingot solid fraction is then obtained through an iterative procedure<sup>1</sup>:

$$[\text{TD}](t_i) = [\text{TD}](t_{i-1}) + G(T(t_i), [O_i])dt, \quad (1)$$

where  $t_i$  and  $t_{i-1}$  denote current and previous time steps and  $dt = t_i - t_{i-1}$  is the time step magnitude.

Veirman et al. [18] introduced this method as a way to assess Cz thermal simulations validity using experimental  $[O_i]$  data. In the present study,  $[O_i]$  measurements were also used as input data and the method was applied to investigate TD formation dynamics. It is worth mentioning that the procedure, as it was implemented, does not account for  $[O_i]$  variations with time resulting from TD generation. We thereby implicitly assumed that solid-state diffusion of  $O_i$  was negligible and that [TD] remained low compared to the initial  $[O_i]$ . This last point may be questionable for high quality materials featuring very low  $[O_i]$ . However, in the present study, [TD] and  $[O_i]$  were in the order of  $10^{15} \text{ cm}^{-3}$  and  $10^{18} \text{ cm}^{-3}$  respectively. Assuming that each TD requires at most 20  $O_i$  atoms, which can be considered as an upper bound [4], then the  $[O_i]$  reduction due to TD formation should be less than 2%. This

<sup>1</sup> For the sake of clarity, all temperature values were reported in °C. However, for all equations  $T$  must be considered in K.

working hypothesis was then considered as valid, but for specific cases with significant  $[O_i]$  reduction, a revision of the computation method might be required. Unless otherwise specified, a time step of 60 s was used for TD formation computations. This value was observed to be sufficiently small to achieve converged values of the final [TD].

### 3.2. Thermo-hydraulic simulations

Ingots thermal histories were obtained from thermo-hydraulic simulations using a Cz furnace model presented in Ref. [18]. The model is axisymmetric and accounts for conductive, convective and radiative heat transfers. Convection was solved in both argon atmosphere and silicon melt. Following Kirpo [21], the Spalart-Allmaras turbulence model was used. A PID regulation was used to adjust the furnace heater power in order to reach the silicon melting temperature at the solid-liquid interface, which was defined as a plane wall. The problem was solved with Ansys Fluent CFD code.

As explained in Ref. [18], ingot thermal histories were obtained from several quasi-steady simulations at different steps of the crystallization process and a transient simulation of the ingot final cooling. The numerical results of the steady-state simulations were linearly interpolated, assuming a prescribed pulling rate, in order to define the ingot temperature evolution in time. In the present study, a particular attention was paid to the pulling rate definition. Time-dependent pulling rates recorded during the experiments were used for the computations. The effect of a constant pulling rate assumption is discussed in section 4.3.

### 3.3. Thermal donors formation models

In the previous paper [18], TD formation computations were based on the model proposed by Wada [5]. In the present study, four models proposed in the literature were compared [5,6,19,20]. These models were selected because they propose a relation  $[TD] = f(T, [O_i], t)$ , which was a prerequisite for our study. Brief descriptions of these models are provided in this section.

#### 3.3.1. Model from Wada [5]

A detailed analysis of Wada [5] TD formation model implementation for Cz growth configurations is provided in Ref. [18]. Contrary to the other models investigated in this study, this model does not predict that TD formation reaches a steady-state regime with constant formation rate for a constant temperature annealing. **The TD concentration is instead expected to follow an exponential law:**

$$[TD](t) = \frac{a}{b} \frac{[O_i]^3}{n^2} \{1 - \exp(-bD_{O_i}[O_i]t)\}, \quad (2)$$

until it reaches a saturation limit defined by:

$$[TD]_{sat} = \frac{a}{b} \frac{[O_i]^3}{n^2}, \quad (3)$$

where  $a$  and  $b$  are constants (cm),  $D_{O_i}$  is the diffusivity of  $O_i$  ( $\text{cm}^2 \text{s}^{-1}$ ), and  $n$  is the electron concentration ( $\text{cm}^{-3}$ ) at  $T$ . In the case of a Cz growth process, where  $T$  is continuously decreasing, it is not obvious to apply the exponential law defined by Eq. (2) and Veirman et al. [18] relied on the initial formation rate:

$$G_W = \left. \frac{d[TD]}{dt} \right|_{t=0} = aD_{O_i} \frac{[O_i]^4}{n^2}. \quad (4)$$

In Eqs. (3) and (4), both  $D_{O_i}$  and  $n$  depend on temperature, and are therefore not constant during the Cz growth process. It should be noted

that a correction factor of 0.75 was proposed in Ref. [18] for TD concentrations predicted by Wada's model. This correction was also applied in the present computations. It is based on a comparison with experimental results obtained for annealing experiments of various Cz silicon materials at 450°C. Veirman et al. [18] also explained that the value used by Wada [5] for the density-of-states effective masses for holes,  $m_{dh}$ , (required to determine the concentration of intrinsically generated free carriers  $n_i$ ) was unclear. The commonly accepted value of  $0.81m_0$ , where  $m_0$  is the electron rest mass, was then adopted.

#### 3.3.2. Model from Voronkov et al. [6]

A semi-empirical model for TD formation was proposed by Voronkov et al. [6]. This model is based on annealing experiments performed on Cz silicon samples pre-annealed at 950°C to eliminate TD formed during crystal growth. The TD formation kinetics observed in Ref. [6] differs from Ref. [5]. A steady-state regime with a constant formation rate is observed after an initial transient and no saturation limit was reported, even for annealing experiments over 30 h. The TD formation process is modeled as a combination of several transitions from  $O_n$  to  $O_{n+1}$ . For each transition a specific reaction rate is defined by:

$$G_{n \rightarrow n+1} = 4\pi r D_{O_n} [O_n][O_i], \quad (5)$$

where  $r$  is the capture radius (cm) and  $D_{O_n}$  is the diffusivity of the  $O_n$  cluster ( $\text{cm}^2 \text{s}^{-1}$ ). The concentration  $[O_n]$  is assumed to be proportional to  $[O_i]^n$ . These reaction rates can then be conveniently expressed as:

$$G_{n \rightarrow n+1} = A_{n \rightarrow n+1} \exp\left(-\frac{E_{n \rightarrow n+1}}{k_B T}\right) [O_i]^{n+1}, \quad (6)$$

where  $A_{n \rightarrow n+1}$  are constants,  $E_{n \rightarrow n+1}$  activation energies (eV) and  $k_B$  the Boltzmann constant ( $\text{eV K}^{-1}$ ). Voronkov et al. [6] consider that limiting fluxes are  $G_{12}$  and  $G_{45}$  for temperatures below 450°C. They also consider that a negative flux must be added to retrieve the decrease of the TD formation rate,  $G_V$ , at higher temperatures. This flux is attributed to either the  $O_7$  to  $O_8$  transition or to an atomic reconfiguration of  $O_8$  clusters. For the sake of simplicity this flux is denoted  $G_{78}$  in the present paper. The flux  $G_{34}$  is also included, even if its influence on  $G_V$  is smaller. Other fluxes are neglected. The TD steady-state formation rate is then defined by:

$$\frac{1}{G_V} = \frac{1}{G_{12}} + \frac{1}{G_{34}} + \frac{1}{G_{45}} + \frac{1}{G_{78}}. \quad (7)$$

The authors explain that their most reliable experimental data were obtained for conditions  $T = 425^\circ\text{C}$  and  $[O_i] = 6.6 \times 10^{17} \text{cm}^{-3}$  (with their FTIR calibration coefficient of  $2.45 \times 10^{17} \text{cm}^{-2}$  [6]). They used these 'standard' conditions to determine reference fluxes values  $G_{n \rightarrow n+1}^0$  and activation energies  $E_{n \rightarrow n+1}$ , through a fitting procedure. The reference fluxes and the activation energies provided in Ref. [6] are listed in Table 2, along with the deduced coefficients  $A_{n \rightarrow n+1}$ .

**Table 2**

Reference fluxes  $G_{n \rightarrow n+1}^0$  at standard conditions, activation energies  $E_{n \rightarrow n+1}$  and deduced coefficients  $A_{n \rightarrow n+1}$ .

	$G_{n \rightarrow n+1}^0$ ( $\text{cm}^3 \text{s}^{-1}$ )	$E_{n \rightarrow n+1}$ (eV)	$A_{n \rightarrow n+1}$
$O_1 \rightarrow O_2$	$1.7 \times 10^{10}$	2.53	$7.159 \times 10^{-8}$ ( $\text{cm}^3 \text{s}^{-1}$ )
$O_3 \rightarrow O_4$	$6.8 \times 10^{10}$	1.1	$3.126 \times 10^{-53}$ ( $\text{cm}^9 \text{s}^{-1}$ )
$O_4 \rightarrow O_5$	$2.9 \times 10^{10}$	0.5	$9.420 \times 10^{-76}$ ( $\text{cm}^{12} \text{s}^{-1}$ )
$O_7 \rightarrow O_8$	$5.5 \times 10^{11}$	-1.7	$8.168 \times 10^{-144}$ ( $\text{cm}^{21} \text{s}^{-1}$ )

<sup>2</sup> In Ref. [5],  $a$  and  $b$  are given in  $\text{cm}^4$ , but it conflicts with units homogeneity for Eqs. (2) and (4). We suggest that  $a$  and  $b$  should be in cm.

**Table 3**

Polynomial coefficients obtained by least squares fitting for the parameters  $\beta(T)$  and  $\alpha(T)$ .

	$\beta(T)$	$\alpha(T)$
$p_0$	$2.016 \times 10^2$	$-3.720 \times 10^3$
$p_1$	$-6.137 \times 10^{-1}$	$1.133 \times 10^1$
$p_2$	$4.704 \times 10^{-4}$	$-8.661 \times 10^{-3}$

### 3.3.3. Model from Londos et al. [19]

Londos et al. [19] performed annealing experiments on Cz samples pre-annealed at 650°C during 30 min to eliminate TD introduced during crystal growth. They observed that [TD] increased linearly during the first part of the annealing. The trend then became non-linear after shorter times for higher annealing temperatures. The TD initial formation rate was found to be proportional to  $[O_i]$  at the power  $\beta$ , where  $\beta$  is a function of the annealing temperature:

$$G_L = \alpha [O_i]^\beta. \quad (8)$$

For the present study, an empirical model was derived from their experimental data. The coefficients  $\beta$  and  $\alpha$  were determined by linear fits (in logarithmic representation) of the formation rates measured at different annealing temperatures. Each coefficient was then defined as a function of the temperature by a second order polynomial fit:

$$f(T) = p_0 + p_1 T + p_2 T^2. \quad (9)$$

The polynomial coefficients are given in Table 3. The model derived from the results presented in Ref. [19] is limited by the investigated temperature range (from 350 to 500°C). A major difficulty for the analysis of TD formation during Cz growth is the extrapolation to higher temperatures, where the formation rate is known to decrease.

### 3.3.4. Model from Åberg et al [20]

Another TD formation model was proposed by Åberg et al. [20], using experimental data from Ref. [22,23]. This kinetic model is based on a reaction scheme including several association and dissociation reactions occurring between oxygen polymers. The model then consists of a differential equations system describing time variations of the different oxygen compounds (see Appendix A). Authors note that TD can represent up to 16 different electrically active defects (from TD1 to TD16). In their model, only TD1 to TD3 are explicitly considered and no specific equation is provided for [TD3]. In the present study, we assumed that other TD families are either negligible or that reactions between these families do not significantly affect the total TD concentration, defined by:

$$[TD] = [TD1] + [TD2] + [TD3]. \quad (10)$$

In the original model [20], the loss of  $O_i$  due to dimers formation is accounted for. However, authors note that the  $[O_i]$  loss observed in their simulations is very low. As mentioned before, the  $[O_i]$  loss due to TD formation was neglected in the present study, as for the other TD formation models. Four annealing temperatures ranging from 350 to 420°C

were investigated in Refs. [20]. Considering that this temperature range is relatively limited and that no obvious extrapolation could be performed, this model was only tested for these four specific temperatures. The differential equations system was numerically solved using a Euler scheme, assuming that oxygen polymers initial concentrations were null. The TD formation dynamics observed in the numerical results was similar to Ref. [6] with a steady-state regime occurring after an initial transient. The initial transient was longer for low annealing temperatures and simulations of long annealing durations were required to determine the steady-state formation rate,  $G_A$ . A linear fit of  $[TD](t)$  for a time interval starting at  $t = 200$  h and ending at  $t = 500$  h was finally used to obtain  $G_A$ .

### 3.3.5. Models comparison

A comparison of the TD formation models [5,6,19,20] is proposed in this section and their main characteristics are summarized in Table 4. As mentioned before, these models focus on constant temperature annealing experiments. Their ability to describe TD formation during a Cz crystallization process is therefore questionable. In the present study, temperature variations were considered to be slow enough for the TD formation kinetics to adapt instantly. The model derived from the experimental results presented in Ref. [19] is completely empirical, whereas the three other models [5,6,20] can be considered as semi-empirical as they propose a theoretical framework for TD formation and rely on experimental data to calibrate some coefficients. The reference experiments were all performed on Cz silicon samples either as-grown [5,22,23] or pre-annealed to eliminate TD formed during growth processes [6,19]. In these studies, samples  $[O_i]$  were measured by FTIR with various calibration coefficients (see Table 4). To compare the TD formation rates predicted by the different models, the same input  $[O_i]$  value must be used. As explained in section 2,  $[O_i]$  values presented in this paper correspond to a FTIR calibration coefficient of  $C_{FTIR}^{SEMI} = 3.14 \times 10^{17} \text{ cm}^{-2}$ . To account for the difference between the FTIR calibration coefficient used for our measurements and the FTIR calibration coefficients to be used for the different models,  $[O_i]$  input values were first multiplied by the ratio  $C_{FTIR}^{model} / C_{FTIR}^{SEMI}$ , where  $C_{FTIR}^{model}$  refers to the FTIR calibration coefficient of the considered model.

Fig. 2 presents the formation rates obtained with the four models as a function of the annealing temperature. The model proposed by Wada [5] leads to larger formation rates and does not predict a decrease at high temperatures. Models from Voronkov et al. [6] and Åberg et al. [20] provide very similar formation rates. The temperature range investigated in Refs. [20] is however too small to observe a decrease at high temperatures. The model from Londos et al. [19] features a similar trend than the model from Voronkov et al. [6] but with a faster decrease at high temperatures and a maximum formation rate occurring at a lower temperature.

Fig. 3 presents the formation rates obtained with the four models as a function of  $[O_i]$ . For  $[O_i] < 10^{18} \text{ cm}^{-3}$ , the models from Wada [5] and Voronkov et al. [6] predict a stronger decrease of the formation rate with  $[O_i]$ . For  $[O_i] > 10^{18} \text{ cm}^{-3}$ , the model from Wada [5] predicts larger formation rates and a faster increase than the three other models which

**Table 4**

Characteristics of the TD formation models and of their underlying experimental data [5,6,19,20]. The reported  $[O_i]$  values were converted for a FTIR calibration coefficient of  $3.14 \times 10^{17} \text{ cm}^{-2}$ .

	Wada [5]	Voronkov et al. [6]	Londos et al. [19]	Åberg et al [20]
nature of the model	semi-empirical	semi-empirical	empirical	semi-empirical
samples pre-treatment	as-grown	pre-annealed	pre-annealed	as-grown
T range (°C)	unspecified	(400–515)	(350–500)	(350–420)
$[O_i]$ range ( $\text{cm}^{-3}$ )	unspecified	$(7.0\text{--}8.5) \times 10^{17}$	$(8.3\text{--}16) \times 10^{17}$	$10 \times 10^{17}$
FTIR coefficient ( $\text{cm}^{-2}$ )	$2.75 \times 10^{17}$	$2.45 \times 10^{17}$	$3.14 \times 10^{17}$	$2.45 \times 10^{17}$



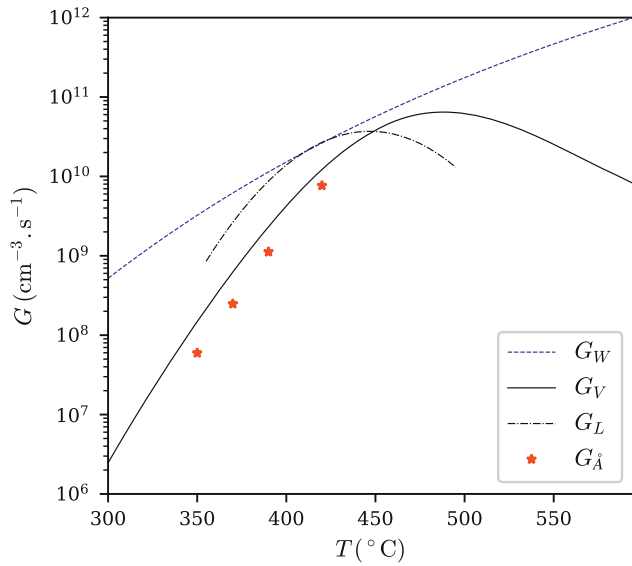


**Fig. 2.** TD formation rates as a function of the annealing temperature. The interstitial oxygen concentration was set to  $[O_i] = \times 10^{18} \text{ cm}^{-3}$  using a FTIR calibration coefficient of  $3.14 \times 10^{17} \text{ cm}^{-2}$ . For  $G_W$  computation, TD contribution to the electron concentration  $n$  was neglected.

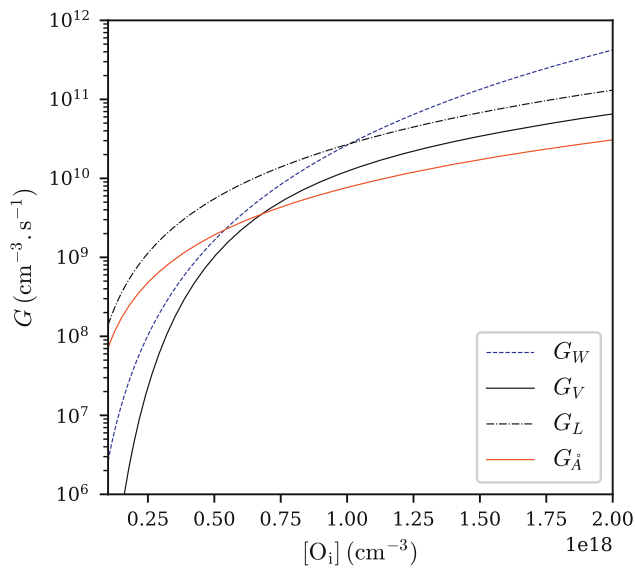


**Fig. 3.** TD formation rates as a function of  $[O_i]$  (using a FTIR calibration coefficient of  $3.14 \times 10^{17} \text{ cm}^{-2}$ ). The temperature was set to  $420^\circ \text{C}$  (i.e. the highest temperature investigated in Refs. [20]).

feature a similar increase with  $[O_i]$ .

Several observations can be made from the models formulations. First, the model from Wada [5] is the only one that does not predict a decrease of the formation rate at high temperatures. However, TD formation is capped by the saturation limit defined by Eq. (3) which decreases with  $T$ . As detailed in the previous paper [18], this saturation limit was implemented in TD formation computations relying on Wada's model. Second, the model from Wada [5] is also the only one considering the dopant concentration as an input parameter. In the other models this parameter is not considered, or is implicitly taken into account by the dopant concentration of the samples used for calibrations [6]. Wada [5] shows that when the dopant concentration is below

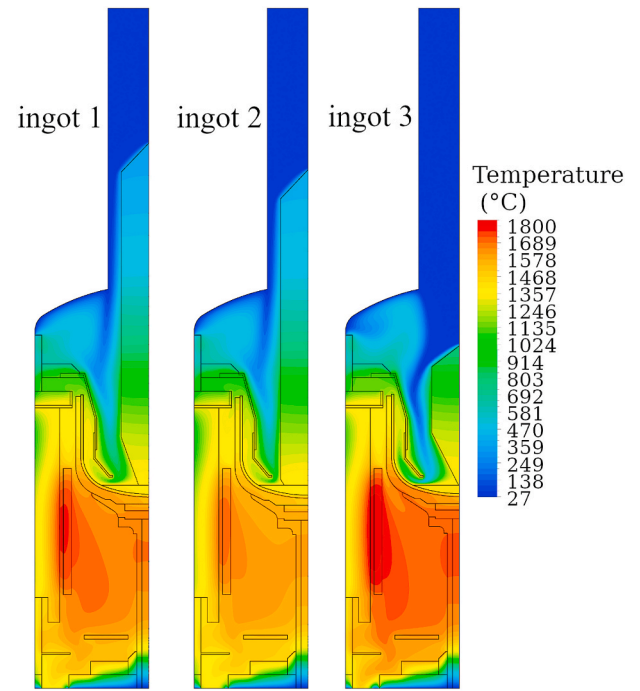


**Fig. 4.** Furnace temperature fields observed in the simulations at the end of the growth step for the three configurations.

$10^{16} \text{ cm}^{-3}$  (for n- or p-type silicon), it has almost no influence on the formation rate  $G_W$  or the saturation limit  $[TD]_{sat}$ , at least at high temperatures (above  $400^\circ \text{C}$ ). The inclusion of this parameter in TD formation computations was therefore not motivated. Third, each study is limited to the temperature and concentration ranges experimentally investigated. Wada [5] and Voronkov et al. [6] propose generic expressions that can be applied to any temperatures and concentrations. For Londo et al. [19] and Åberg et al. [20], relations are only given for specific temperatures and a rather awkward extrapolation procedure should be adopted in order to apply these models to Cz growth configurations. For this reason, only Wada [5] and Voronkov et al. [6] models were eventually implemented for TD computations during Cz growth. Finally, the model from Voronkov et al. [6] only provides a steady-state formation rate. In the present study, it was assumed that the initial transient occurring in TD formation during a constant temperature annealing could be neglected in the case of a Cz process. This assumption is supported by the fact that the initial transient becomes relatively short for high temperatures, as shown by Voronkov et al. [6] experimental results for annealing at  $425^\circ \text{C}$  and the TD formation dynamics observed in the model from Åberg et al. [20] (see section Appendix A). During a Cz process, the silicon is progressively cooled from its melting point (i.e.  $1414^\circ \text{C}$ ) and invariably meet temperatures close to  $470^\circ \text{C}$  where a strong TD production is expected, as well as a short transient phase for TD formation. It then appears reasonable to consider that the main part of TD production occurs in a quasi-steady regime during a Cz process. Considering further the initial transients observed in constant temperature annealing experiments, a legitimate question is whether similar transients can exist during a Cz process. A major difference between the two configurations is that in annealing experiments the material is initially at room temperature, whereas during a Cz process it is cooled from its melting point and only meets high temperatures before it reaches optimal TD formation temperatures (around  $470^\circ \text{C}$ ). If TD formation transients exist in Cz growth, they may be very different from initial transients observed in annealing experiments, both in nature and in duration. Valuable information could be gathered from annealing experiments with time varying temperature imitating a Cz process. Unfortunately, to our knowledge, such experiments have not been reported

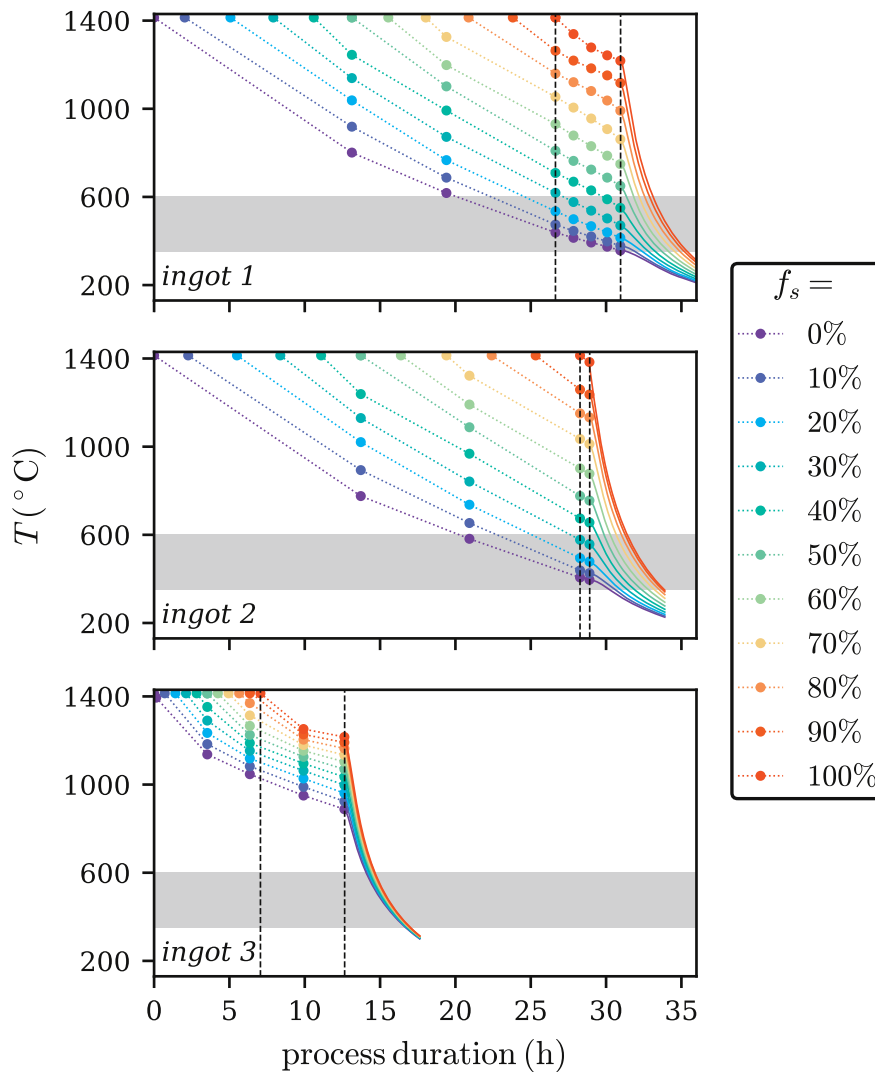


**Fig. 5.** Thermal histories of the three ingots. The dashed lines represent the beginning and the end of the tailing step. The grey area represents the TD formation temperature range (from 350 to 600°C). The initial time,  $t = 0$ , is defined as the ingot body growth start. The points (·) represent the temperatures observed in the steady-state simulations for each solid fraction, and the dotted lines represent the linear interpolation used for thermal histories reconstruction. The solid lines represent the temperature evolution observed in the transient cooling simulations for each solid fraction.

yet.

## 4. Results and discussion

### 4.1. Ingots thermal histories

Specific thermo-hydraulic simulations were performed for the three experimental configurations, accounting for the different ingot geometries and process parameters. The temperature fields obtained at the end of the crystallization step are presented in Fig. 4 and the thermal histories are presented in Fig. 5. Major differences can be observed on the thermal histories experienced by the three ingots. First, compared to ingot 1, the body growth step of ingot 2 was 1.6 h (i.e. 6%) longer owing to ingot diameter and growth rate variations. Second, the tailing step was reduced from 4.3 h for ingot 1 to 39 min for ingot 2 due to pop out. As a consequence, the upper part of ingot 2 spent less time in the TD formation temperature range (from 350 to 600°C), and the body fraction to enter this temperature range before the cooling step was smaller than for ingot 1. Finally, unlike ingots 1 and 2, ingot 3 was short enough to remain above the TD formation temperature range until tailing was completed. Indeed, at the end of the crystallization step, the temperature at the top of the ingot was 343°C for ingot 1, 377°C for ingot 2 and 791°C for ingot 3.

### 4.2. TD formation dynamics

The TD concentration profiles obtained by simulations with the model from Wada [5] and the model from Voronkov et al. [6] are presented in Fig. 6, along with the experimental data. Focusing on ingot 1, the concentration profile can be split into three parts: an upper part ( $f_s < 20\%$ ) with large and almost constant TD concentrations, a transition area ( $20\% \leq f_s \leq 45\%$ ) where concentrations rapidly decrease, and a lower part ( $f_s > 45\%$ ) with low concentrations slowly decreasing towards the ingot tail. Numerical computations using the TD formation model from Voronkov et al. [6] are in remarkable agreement with the experimental values for the first and third parts, with a relative deviation below 15% for the first part and 25% for the third part. The rapid transition of the second part was qualitatively retrieved in the numerical results but occurred later than in the experimental data. This difference may be ascribed to thermal simulations approximations (like external thermal boundary conditions definition or the assumption of a 2D-axisymmetric convection flow), and is further discussed in the next paragraph. Numerical computations using the TD formation model from Wada [5], modified according to Ref. [18] with a 0.75 correction factor, provided a good estimate of TD concentrations for the ingot first part, but they significantly overestimated them in the second and third parts. A similar behavior was observed for ingot 2. Compared to ingot 1, lower

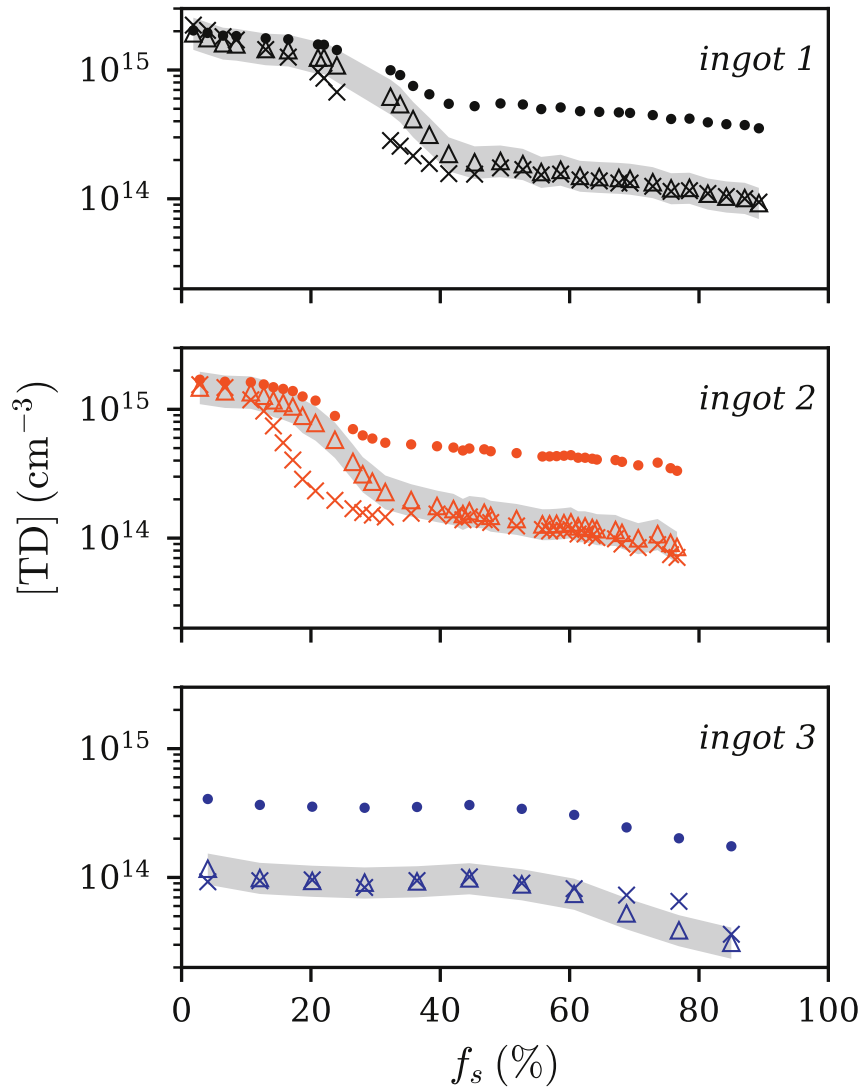


**Fig. 6.** TD concentrations along the three ingots, with  $f_s$  the fraction of the ingot body length. Crosses ( $\times$ ) represent experimental values, points ( $\cdot$ ) numerical values obtained with the model from Wada [5] and triangles ( $\triangle$ ) numerical values obtained with the model from Voronkov et al. [6]. Grey bands represent numerical [TD] variations obtained for input  $[O_i]$  variations of  $\pm 5\%$ , with the model from Voronkov et al. [6]

[TD] values were observed all along the axial profile of ingot 2. For instance [TD] was reduced by 23% on average in the lower part. Moreover, the rapid transition occurred earlier ( $f_s \approx 10\%$ ) than for ingot 1. These effects can be ascribed to the reduction of  $[O_i]$  but also to the different thermal history experienced by ingot 2, and particularly to the tailing step removal. This last point is further discussed in the next paragraph. The relative deviation between [TD] measurements and computations, based on the model from Voronkov et al. [6], was also limited to 15% for the first part of ingot 2, and to 25% for the third part. For ingot 3, [TD] was more uniform along the ingot body and lower than for ingots 1 and 2. These results are consistent with the lower and more uniform  $[O_i]$  profile observed in ingot 3 (Fig. 1), and its shorter thermal history in the TD formation temperature range (Fig. 5). Here, the relative deviation between measured and computed [TD] values was limited to 30% on the whole ingot, excepted for one solid fraction where it reached 40%. Based on these first results, the model from Voronkov et al. [6] was preferred to the model from Wada [5] for TD formation computations and was retained for the rest of the study.

These overall good agreements between simulations and experiments led us to trust further simulation outputs to discriminate TD

formed during crystallization and cooling steps. Fractions of TD formed during the cooling step along the three ingots are presented in Fig. 7. For ingots 1 and 2, the upper part corresponds to TD mostly formed during the growth step and the lower part corresponds to TD mostly formed during the cooling. As mentioned before, the temperature of ingot 3 remained above the TD formation range during the growth step and TD were formed only during the cooling step. The transitions observed in Fig. 6 for ingots 1 and 2 reflect the area where the growth step contribution to TD formation progressively became negligible compared to the cooling step contribution. The position of this transition in the ingot is controlled by the vertical thermal gradient occurring in the furnace. Indeed, the thermal configuration defines the area where the ingot crosses the TD formation temperature range (from 350 to 600°C) during the growth step. The transition then occurs in the ingot region located just below this area at the end of the growth step, since the fraction of TD formed during the growth step is strongly reduced (implying that the lower part of the ingot remained above 600°C until its final cooling). In the present study, the calibration of the thermal model was not precise enough to reproduce exactly the thermal gradient occurring in the furnace, resulting in a shift of the [TD] transition. A more accurate

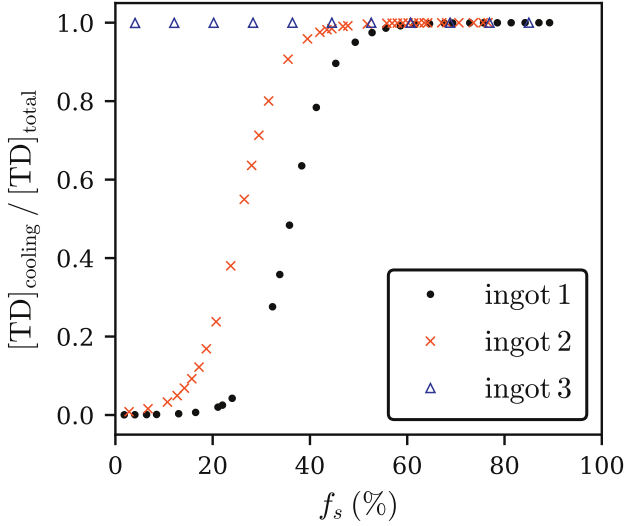


**Fig. 7.** Ratio between concentrations of TD formed during ingot cooling and total TD concentrations.

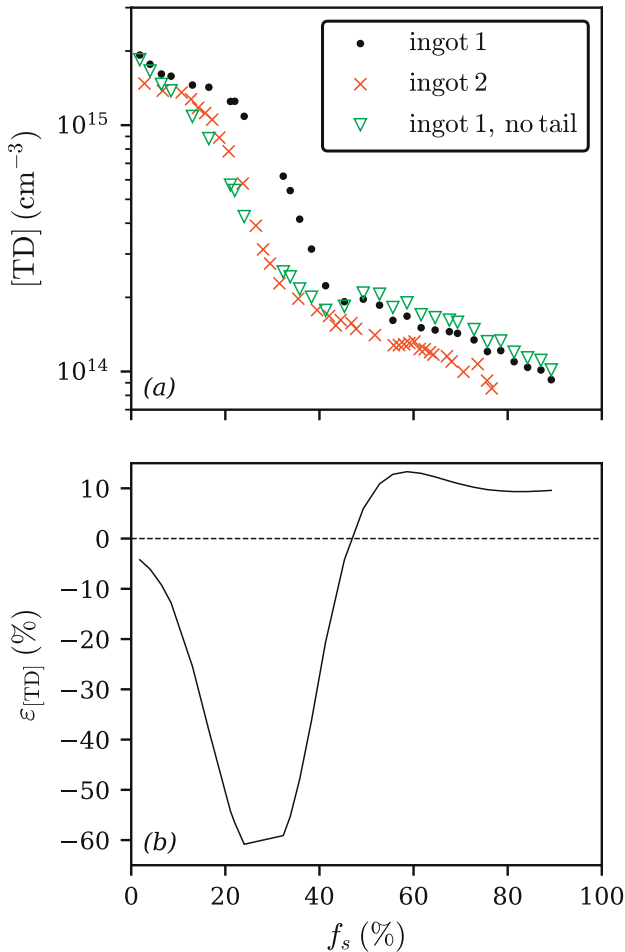


**Fig. 8.** Axial [TD] profiles for ingots 1, 2 and 1 without tailing step (a); and relative deviation of [TD],  $\epsilon_{[TD]} = \{[TD]_1^{no\ tail} - [TD]_1\} / [TD]_1$ , induced by the removal of the tailing step for ingot 1 (b).

calibration of the thermal model could be achieved with in-situ temperature measurements in the upper part of the furnace. The earlier transition observed for ingot 2, compared to ingot 1, can be explained by the reduction of the tailing step, which prevented a larger part of the ingot to enter the TD formation range before the cooling step. To confirm this assumption, specific simulations were performed to obtain the thermal history of ingot 1 without the tailing step. This result allowed us to quantify the effect of the tailing step on the axial [TD] profile. First, without tailing the transition occurred earlier and matched the transition of ingot 2, as observed in Fig. 8(a). The shift of the transition area resulted in a large reduction of [TD] for  $10\% \leq f_s \leq 45\%$ . Second, in the lower part of the ingot ( $f_s > 45\%$ ), [TD] increased by around 10% on average (see Fig. 8(b)). This increase of TD formed during the cooling step can be explained by the reduction of the ingot total length due the removal of the tail. Indeed, the shorter length implied a lower position of the ingot in the furnace during the cooling step, and owing to the vertical thermal gradient occurring in the furnace, the cooling of the lower part of the ingot was slowed down. This last point also confirmed that the lower [TD] observed for the lower part of ingot 2 (compared to ingot 1) were due to the reduction of  $[O_i]$ , and not to the change of thermal history, since the removal of the tailing step resulted in an increase and not a decrease of [TD] in the lower part of ingot 1.

#### 4.3. Sensitivity analyses

Finally, sensitivity analyses were carried out to assess the reliability of the method. First, the effect of small variations of the input  $[O_i]$  on the final [TD] was analyzed. Relative variations of  $\pm 5\%$  were applied to  $[O_i]$  experimental values. The value of  $\pm 5\%$  represents the upper bound of OxyMap measurements uncertainties [10]. Resulting variations of the computed [TD] along the three ingots are presented in Fig. 6. Maximum and minimum relative deviations observed along the three ingots are reported in Table 5. As expected, the method is highly sensitive to the  $[O_i]$  input value, and the larger deviations occurred for ingot 2 with [TD] variations up to 36.5 and  $-27.8\%$ .

Second, the sensitivity to the thermal history accuracy was investigated. Several parameters can affect the ingot thermal history, among which: the furnace material properties, the heaters power, the pulling rate, the ingot geometry or the gas and melt convection flows. In this study, we focused on the ingot pulling rate which is a key parameter to define the ingot temperature variations during the crystallization step. In our first paper [18], the TD computation procedure was simplified by the assumption of a constant pulling rate. In practice, the pulling rate fluctuates during a Cz process and will inevitably show ingot-to-ingot variations even for a given pulling process. Therefore, it is critical to assess the sensitivity to such variability of the output [TD] profiles along the ingot. As mentioned in section 3, for the present study time-varying pulling rates recorded during the experiments were used to assemble ingots thermal histories. As an example, the pulling rate profile used for ingot 1 is presented in Fig. 9. During the body growth step, a rapid decrease of the pulling rate was first observed (for  $x \leq 0.1$  m), followed by pseudo-periodic fluctuations due to the automatic regulation. The pulling rate then rapidly increased during the tailing step. For the given geometry of ingot 1, the assumption of a constant pulling rate, equal to the mean experimental value, would lead to a reduction by 16 min (i.e. 1%) of the body growth step duration, and an increase of 28 min (i.e. 11%) of the tailing step duration.

**Table 5**

Maximum and minimum relative deviation of [TD] induced by a variation of  $[O_i]$  of  $\pm 5\%$ ,  $\epsilon = \{[TD]([O_i] \pm 5\%) - [TD]\} / [TD]$ , along the three ingots.

	$\epsilon_{max}$ (%)	$\epsilon_{min}$ (%)
ingot 1	36.1	-27.7
ingot 2	36.5	-27.8
ingot 3	31.2	-24.8



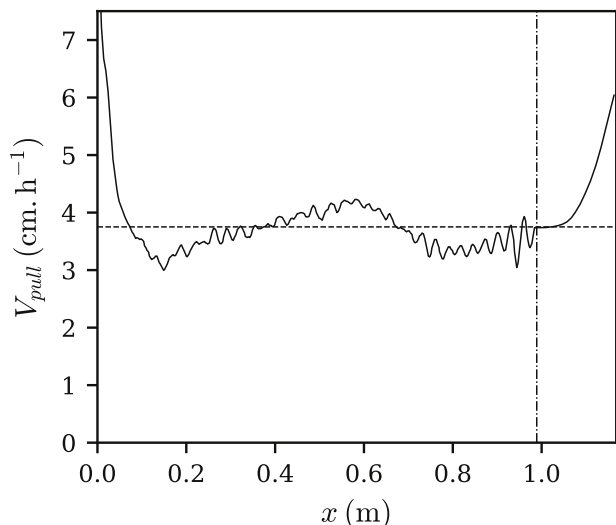


**Fig. 9.** Experimental pulling rate applied for ingot 1 during body and tail growth. The abscissa  $x$  represents the ingot longitudinal coordinates, with  $x = 0$  the beginning of the ingot body. The horizontal dashed line represents the mean pulling rate and the vertical dashed line represents the beginning of the tail.

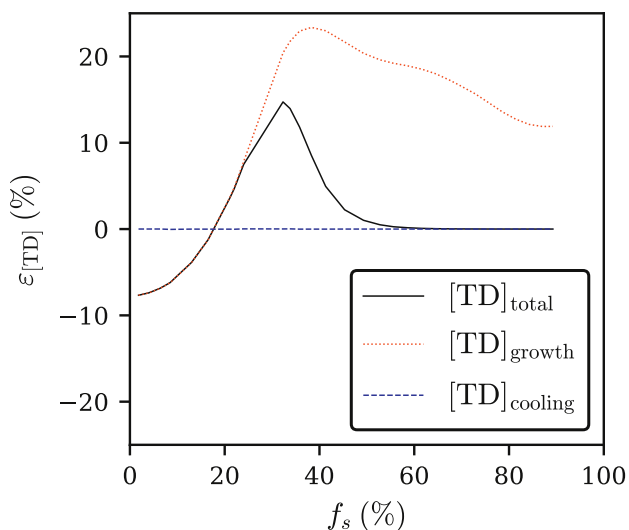


**Fig. 10.** Relative deviation between TD concentrations computed with a constant pulling rate and TD concentrations computed with the experimental pulling rate values,  $\varepsilon_{[TD]} = \{[TD]_{\text{constant rate}} - [TD]_{\text{variable rate}}\} / [TD]_{\text{variable rate}}$ , for the ingot 1.

The influence of such modifications of the body growth and tailing steps durations on the TD formation was then assessed. The relative deviation between TD concentrations computed with a constant or a variable pulling rate is presented in Fig. 10. As expected, the constant pulling rate assumption had no influence on TD formed during the cooling step, as this parameter can only affect the crystallization step. A strong influence on the TD formed during the growth step was observed, especially in the transition area ( $20\% \leq f_s \leq 40\%$ ) with up to 23% of relative deviation from the variable pulling rate case. The relative deviation on the total TD concentration was however limited to 15%. Note that, for this particular test, the numerical time step used to compute

[TD] was reduced from 60 s to 1 s in order to decrease residual errors that can affect very small values of  $[TD]_{\text{growth}}$  occurring on the ingot final part ( $f_s > 40\%$ ) and of  $[TD]_{\text{cooling}}$  occurring in the first parts ( $f_s < 40\%$ ). These results highlight that even if a constant pulling rate assumption can be used as a first approximation to estimate TD formed during a Cz crystallization process, it can lead to significant errors depending on the actual pulling rate applied in practice. Special attention should be paid to pulling rate variations occurring at the end of the body growth step and during the tailing step. These are critical steps for TD formation since a significant part of the ingot can be in the TD formation temperature range. A precise estimation of the time spent in this temperature interval is then required for an accurate computation of the final [TD].

## 5. Conclusions

In the present study, the computation method developed by Veirman et al. [18] for TD formation during Cz growth was improved thanks to the implementation of the TD formation model proposed by Voronkov et al. [6]. The method was applied to three experimental configurations and a remarkable agreement was observed between measured and computed TD concentrations, demonstrating its robustness. The numerical model was used to explain the TD formation dynamics during Cz growth and to discriminate TD formed during crystallization or cooling steps. Finally, the sensitivity of the computation method to  $[O_i]$  variations and pulling rate definition was quantified. Results showed that the input  $[O_i]$  was critical for accurate [TD] computations, and that the definition of a time-varying or constant pulling rate could have a significant effect on [TD]. This method proved to be a promising tool for future improvements of Cz growth processes for solar cells production. In this respect, the effect on the TD concentration of a pop-out for a given process or the addition of cooling elements in a furnace could be rapidly estimated. An interesting and challenging perspective is the development of a fully predictive model including numerical simulations of oxygen transport and its incorporation into the ingot during crystallization, as proposed by several authors [21,24–26]. Such a model would bypass the need to use experimental  $[O_i]$  as inputs.

## CRedit authorship contribution statement

**M. Chatelain:** Conceptualization, Software, Validation, Investigation, Writing - original draft. **M. Albaric:** Conceptualization, Software, Resources, Writing - review & editing. **D. Pelletier:** Conceptualization, Software, Writing - review & editing. **J. Veirman:** Conceptualization, Methodology, Validation, Investigation, Writing - review & editing. **E. Letty:** Conceptualization, Methodology, Software.

## Declaration of competing interest

The authors declare that they have no known competing financial interests or personal relationships that could have appeared to influence the work reported in this paper.

## Acknowledgments

This work is a continuation of a former project supported by the State Program “Investment for the Future” bearing the reference (ANR-10-ITE-0003) which allowed the development of a first version of the numerical model. The authors would like to thank E. Fayard, J. Stadler, S. Bailly and S. Rousseau for the crystallization experiments and the FTIR measurements; and W. Favre for many fruitful discussions on this subject.

## Appendix A. Details on the TD formation model from Åberg et al. (1998)

The differential equations system used in the model from Åberg et al. [20] is reported below:

$$\frac{d[\text{TD1}]}{dt} = 4\pi R_{22} D_{\text{O}_2} [\text{O}_2]^2 - A(T)[\text{TD1}] - A_{\text{TD1}}[\text{TD1}], \quad (\text{A.1})$$

$$\frac{d[\text{TD2}]}{dt} = A(T)[\text{TD1}] - A_{\text{TD2}}[\text{TD2}] - 4\pi R_{24} D_{\text{O}_2} [\text{O}_2][\text{TD2}], \quad (\text{A.2})$$

$$\begin{aligned} \frac{d[\text{O}_2]}{dt} = & 4\pi R_{11} D_{\text{O}_i} [\text{O}_i]^2 - 8\pi R_{22} D_{\text{O}_2} [\text{O}_2]^2 - A_{\text{O}_2 \rightarrow \text{O}_2^*} [\text{O}_2] + A_{\text{O}_2^* \rightarrow \text{O}_2} [\text{O}_2^*] \\ & + 2A_{\text{TD1}}[\text{TD1}] + 2A_{\text{TD2}}[\text{TD2}] \\ & - 4\pi R_{24} D_{\text{O}_2} [\text{O}_2][\text{TD2}] - 4\pi R_{26} D_{\text{O}_2} [\text{O}_2][\text{O}_6], \end{aligned} \quad (\text{A.3})$$

$$\frac{d[\text{O}_2^*]}{dt} = A_{\text{O}_2 \rightarrow \text{O}_2^*} [\text{O}_2] - A_{\text{O}_2^* \rightarrow \text{O}_2} [\text{O}_2^*], \quad (\text{A.4})$$

$$\frac{d[\text{O}_6]}{dt} = 4\pi R_{24} D_{\text{O}_2} [\text{O}_2][\text{TD2}] - 4\pi R_{26} D_{\text{O}_2} [\text{O}_2][\text{O}_6], \quad (\text{A.5})$$

$$\frac{d[\text{TD3}]}{dt} = 4\pi R_{26} D_{\text{O}_2} [\text{O}_2][\text{O}_6]. \quad (\text{A.6})$$

In this system, TD1, TD2 and TD3 refer to the three TD families considered in the model (over the 16 families mentioned in Ref. [20]); and  $\text{O}_2^*$  refers to the immobile oxygen dimer, as opposed to the fast diffusing dimer  $\text{O}_2$ . The values of the diffusivities and of the reactions coefficients are reported in Table A.6. Following [20], the capture radius  $R_{11}$  was considered equal to 7 Å and the value of 5 Å was used for all other capture radii. TD concentrations evolutions during constant temperature annealing obtained with this model are presented in Fig. A.11. The dotted lines represent the linear regression used to determine the steady-state formation rate.

**Table A.6**

Values of the temperature dependent coefficients provided in Ref. [20] for the four annealing temperatures investigated. Note that the value of  $D_{\text{O}_i}$  at 370°C was corrected from  $2.098 \times 10^{-22}$  (given in TABLE I from Refs. [20]) to  $2.098 \times 10^{-21} \text{ cm}^2 \text{ s}^{-1}$ , relying on Eq. (1) from Ref. [20].

	350°C	370°C	390°C	420°C
$D_{\text{O}_i} (\text{cm}^2 \text{ s}^{-1})$	$4.816 \times 10^{-22}$	$2.098 \times 10^{-21}$	$8.36 \times 10^{-21}$	$5.727 \times 10^{-20}$
$D_{\text{O}_2} (\text{cm}^2 \text{ s}^{-1})$	$8 \times 10^{-15}$	$2.4 \times 10^{-14}$	$4.8 \times 10^{-14}$	$8.8 \times 10^{-14}$
$A_{\text{O}_2 \rightarrow \text{O}_2^*} (\text{s}^{-1})$	$7 \times 10^{-6}$	$1 \times 10^{-5}$	$1 \times 10^{-5}$	$1 \times 10^{-5}$
$A_{\text{O}_2^* \rightarrow \text{O}_2} (\text{s}^{-1})$	$8 \times 10^{-6}$	$1 \times 10^{-5}$	$2 \times 10^{-5}$	$3 \times 10^{-5}$
$A (\text{s}^{-1})$	$6 \times 10^{-6}$	$2.87 \times 10^{-5}$	$1.98 \times 10^{-5}$	$7.78 \times 10^{-4}$
$A_{\text{TD1}} = A_{\text{TD2}} (\text{s}^{-1})$	$7 \times 10^{-8}$	$5 \times 10^{-7}$	$3 \times 10^{-6}$	$2.8 \times 10^{-6}$

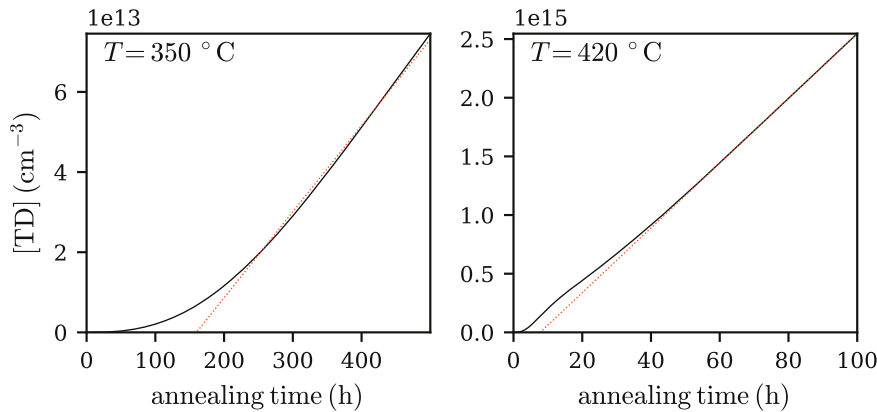


**Fig. A.11.** TD concentrations as a function of the annealing time obtained with the model from Åberg et al. [20], for annealing temperatures of 350°C (left) and 420°C (right). The interstitial oxygen concentration was set to  $[\text{O}_i] = 10^{18} \text{ cm}^{-3}$ , using a FTIR calibration coefficient of  $3.14 \times 10^{17} \text{ cm}^{-2}$ .

## References

- [1] J. Zhao, M. König, Y. Yao, Y. Wang, R. Zhou, T. Xie, H. Deng, 24% silicon heterojunction solar cells on Meyer Burger's on mass production tools and how wafer material impacts cell parameters, in: 2018 IEEE 7th World Conference on Photovoltaic Energy Conversion (WCPEC) (A Joint Conference of 45th IEEE PVSC, 28th PVSEC & 34th EU PVSEC), IEEE, 2018, pp. 1514–1519, <https://doi.org/10.1109/PVSC.2018.8547908>.
- [2] M. Tomassini, J. Veirman, R. Varache, E. Letty, S. Dubois, Y. Hu, Ø. Nielsen, Recombination activity associated with thermal donor generation in monocrystalline silicon and effect on the conversion efficiency of heterojunction solar cells, *J. Appl. Phys.* 119 (2016), 084508, <https://doi.org/10.1063/1.4942212>.
- [3] J. Veirman, R. Varache, A. Danel, M. Albaric, E. Letty, B. Martel, C. Roux, Early efficiency prediction of silicon heterojunction cells processed on thermal donor-rich Czochralski wafers, in: 33rd European Photovoltaic Solar Energy Conference

- and Exhibition, 2017, p. 391, <https://doi.org/10.4229/eupvsec20172017-2co.10.2>.
- [4] P. Wagner, J. Hage, Thermal double donors in silicon, *Appl. Phys. Solid Surface*. 49 (1989) 123–138, <https://doi.org/10.1007/BF00616290>.
- [5] K. Wada, United model for formation kinetics of oxygen thermal donors in silicon, *Phys. Rev. B* 30 (10) (1984) 5884–5895, <https://doi.org/10.1103/PhysRevB.30.5884>.
- [6] V.V. Voronkov, G.I. Voronkova, A.V. Batunina, V.N. Golovina, R. Falster, M. Cornara, N.B. Tiurina, A.S. Guliaeva, Properties of fast-diffusing oxygen species in silicon deduced from the generation kinetics of thermal donors, *Solid State Phenom.* 156–158 (2009) 115–122, <https://doi.org/10.4028/www.scientific.net/SSP.156-158.115>.
- [7] V. Cazcarra, P. Zunino, Influence of oxygen on silicon resistivity, *J. Appl. Phys.* 51 (1980) 4206–4211, <https://doi.org/10.1063/1.328278>.
- [8] L. Chen, X. Yu, P. Chen, P. Wang, X. Gu, J. Lu, D. Yang, Effect of oxygen precipitation on the performance of Czochralski silicon solar cells, *Sol. Energy Mater. Sol. Cell.* 95 (2011) 3148–3151, <https://doi.org/10.1016/j.solmat.2011.06.044>.
- [9] D. Yang, D. Li, L. Wang, X. Ma, D. Que, Oxygen in Czochralski silicon used for solar cells, *Sol. Energy Mater. Sol. Cell.* 72 (2002) 133–138, [https://doi.org/10.1016/S0927-0248\(01\)00158-1](https://doi.org/10.1016/S0927-0248(01)00158-1).
- [10] J. Veirman, B. Martel, N. Enjalbert, S. Dubois, C. Picoulet, P. Bonnard, Oxygen-defect characterization for improving R&D relevance and Cz-Si solar cell efficiency, *Photovoltaics Int.* 33 (2016). <https://store.pv-tech.org/store/oxygendefect-characterization-for-improving-rd-relevance-and-czsi-solar-cell-efficiency/>.
- [11] J. Li, X. Yu, S. Yuan, L. Yang, Z. Liu, D. Yang, Effects of oxygen related thermal donors on the performance of silicon heterojunction solar cells, *Sol. Energy Mater. Sol. Cell.* 179 (2018) 17–21, <https://doi.org/10.1016/j.solmat.2018.02.006>.
- [12] J. Haunschild, J. Broisch, I. Reis, S. Rein, Cz-silicon wafers in solar cell production: efficiency-limiting defects and material quality control, *Photovoltaics Int.* 15 (2012). <http://publica.fraunhofer.de/documents/N-203809.html>.
- [13] J. Veirman, B. Martel, E. Letty, R. Peyronnet, G. Raymond, M. Cascant, N. Enjalbert, A. Danel, T. Desrues, S. Dubois, C. Picoulet, X. Brun, P. Bonnard, Thermal History Index as a bulk quality indicator for Czochralski solar wafers, *Sol. Energy Mater. Sol. Cell.* 158 (2016) 55–59, <https://doi.org/10.1016/j.solmat.2016.05.051>.
- [14] W. Nam, Y. Hahn, S. Baik, Local optimization of graphite heater to save a power consumption of Czochralski Si ingot grower for PV application, *Energy Procedia* 124 (2017) 767–776, <https://doi.org/10.1016/j.egypro.2017.09.083>.
- [15] J. Ding, L. Liu, W. Zhao, Enhancement of heat transfer in Czochralski growth of silicon crystals with a chemical cooling technique, *J. Cryst. Growth* 468 (2017) 894–898, <https://doi.org/10.1016/j.jcrysgro.2016.11.036>.
- [16] ITRPV, International Technology Roadmap for Photovoltaic Results 2018, Tech. rep., 2019 <https://itrvp.vdma.org/>.
- [17] E. Letty, Identification and Neutralization of Lifetime-Limiting Defects in Czochralski Silicon for High Efficiency Photovoltaic Applications, Ph.D. thesis, National Institute for Applied Sciences (INSA), Lyon, France, 2017, <http://www.theses.fr/2017LYSEI094/document>.
- [18] J. Veirman, E. Letty, W. Favre, M. Albaric, D. Pelletier, M. Lemiti, Novel way to assess the validity of Czochralski growth simulations, *Phys. Status Solidi* 216 (17) (2019) 1900317, <https://doi.org/10.1002/pssa.201900317>.
- [19] C.A. Londos, M.J. Binns, A.R. Brown, S.A. McQuaid, R.C. Newman, Effect of oxygen concentration on the kinetics of thermal donor formation in silicon at temperatures between 350 and 500 °C, *Appl. Phys. Lett.* 62 (13) (1993) 1525–1526, <https://doi.org/10.1063/1.108628>.
- [20] D. Åberg, B.G. Svensson, T. Hallberg, J.L. Lindström, Kinetic study of oxygen dimer and thermal donor formation in silicon, *Phys. Rev. B* 58 (19) (1998) 12944–12951, <https://doi.org/10.1103/PhysRevB.58.12944>.
- [21] M. Kirpo, Global simulation of the Czochralski silicon crystal growth in ANSYS FLUENT, *J. Cryst. Growth* 371 (2013) 60–69, <https://doi.org/10.1016/j.jcrysgro.2013.02.005>.
- [22] J.L. Lindström, T. Hallberg, Vibrational infrared-absorption bands related to the thermal donors in silicon, *J. Appl. Phys.* 77 (6) (1995) 2684–2690, <https://doi.org/10.1063/1.358736>.
- [23] T. Hallberg, J.L. Lindström, Infrared vibrational bands related to the thermal donors in silicon, *J. Appl. Phys.* 79 (10) (1996) 7570–7581, <https://doi.org/10.1063/1.362413>.
- [24] J. Chen, Y. Teng, W. Wun, C. Lu, H. Chen, C. Chen, W. Lan, Numerical simulation of oxygen transport during the CZ silicon crystal growth process, *J. Cryst. Growth* 318 (2011) 318–323, <https://doi.org/10.1016/j.jcrysgro.2010.11.145>.
- [25] A. Smirnov, V. Kalaev, Development of oxygen transport model in Czochralski growth of silicon crystals, *J. Cryst. Growth* 310 (2008) 2970–2976, <https://doi.org/10.1016/j.jcrysgro.2008.03.002>.
- [26] L. Liu, S. Nakano, K. Kakimoto, Investigation of oxygen distribution in electromagnetic CZ-Si melts with a transverse magnetic field using 3d global modeling, *J. Cryst. Growth* 299 (2007) 48–58, <https://doi.org/10.1016/j.jcrysgro.2006.10.247>.